International Communications in Heat and Mass Transfer 141 (2023) 106564

Contents lists available at ScienceDirect

International Communications in Heat and Mass Transfer

journal homepage: www.elsevier.com/locate/ichmt

Fully-resolved numerical simulations of the turbulent flow and particle deposition in a cubical cavity with two pairs of differentially heated opposed walls at Rayleigh number 3.6×10^9

Akim Lavrinenko *, Ferran Gisbert, Jordi Pallares, Alexandre Fabregat

Universitat Rovira i Virgili, Departament d`Enginyeria Mecanica, Av. Països Catalans 26, Tarragona 43007, Catalonia, Spain

ARTICLE INFO

Keywords:
Turbulent mixing
Direct Numerical Simulation
Dispersed multiphase flows
Particle wall deposition
Natural convection
Cubical cavity

ABSTRACT

The turbulent dispersion and deposition of airborne solid particles is studied by means of fully-resolved numerical simulations. The computational domain, consisting in a cubical cavity with differentially heated opposed walls filled with air, reproduces the experimental conditions of measurements previously reported in the literature. The computational model assumes that each solid spherical particle trajectory is governed by the balance between hydrodynamic drag, buoyancy, lift, thermophoresis and Brownian forces. The dominant terms responsible for particle deposition mostly depend on the particle size, the solid–gas density ratio and the hydrodynamics within the thermal and momentum boundary layers near the solid surfaces. The present results suggest that previous correlations for the wall-averaged Nusselt number as a function of Rayleigh number over the range between 10^7 and 5.4×10^8 can be extended up to Rayleigh number 3.6×10^9. Also, numerical predictions of the particle deposition rates on thermally active surfaces are in good agreement with both experimental data and analytical boundary layer solutions for particle sizes ranging between 0.1 μm and 2.5 μm in diameter. These particle sizes allows to study different particle deposition regimes varying from that controlled by thermophoresis (0.1 μm) to that dominated by gravitational forces (2.5 μm).

1. Introduction

The present work aims to simultaneously delve into two relevant problems that have garnered significant amount of both numerical and experimental efforts, namely, airborne particle dispersion and turbulent natural convection in enclosed domains. Combined or independently, both topics are of relevance in a wide range of applications including airborne transmission of infectious diseases [1,2], valuable surface soiling [3], formation of blood vessel occlusions [4], oceanic and atmospheric pollutant transport [5], nuclear power plant safety [6] and heat transfer equipment design [7] to mention a few.

Regarding buoyancy-driven flows in enclosed domains, when the Rayleigh number is large enough, even simple geometries consisting in cavities with differentially heated walls exhibit complex flow dynamics characterized by large-scale and coherent circulating structures and non-isotropic small-scale turbulence associated to the presence of momentum and thermal boundary layers in the near-wall regions [8]. Prototypical flow configurations enclosed in parallelepipedic or cylindrical domains and their variants in terms of cavity geometry and thermal wall arrangement have been the subject of both computational and experimental investigations. In their exhaustive review on turbulent natural convection in rectangular cavities, Miroshnichenko and Sheremet [9] concluded that gaining insight into strategies and mechanism to enhanced turbulent heat transfer is crucial given the overwhelmingly large number of real-world applications. The laminar natural convection flows were investigated by Pandey et al. [10] who summarized existing numerical and experimental studies in several types of enclosures with and without internal bodies. Likewise, Abdulkadhim et al. [11] examined natural convection works addressed to investigate more complex geometries.

In this study we focus our attention on the enclosed flow bounded by two pairs of differentially heated opposed walls. This flow configuration was investigated by Shiralkar and Tien [12] who numerically studied the circulating flow in a squared two dimensional (2D) cavity at several Rayleigh numbers (Ra) between 10^3 and 10^6. These authors reported that the numerically predicted streamline patterns were in good qualitative agreement with the experiments by Ostrach and Raghavan [13]. Corcione [14], who numerically studied heat transfer in 2D rectangular enclosures, reported dimensionless correlations and distributions of

* Corresponding author.
E-mail address: akim.lavrinenko@urv.cat (A. Lavrinenko).

https://doi.org/10.1016/j.icheatmasstransfer.2022.106564
Received 9 September 2022; Received in revised form 8 November 2022; Accepted 4 December 2022
Available online 23 December 2022

Nomenclature

Symbols

Ra	Rayleigh number
Nu	Nusselt number
T	temperature
l	length
t	time
u_i	i-th direction velocity
u	velocity
p	pressure
Pr	Prandtl number
g	gravitational acceleration
x_i^*	i-th particle position
u_i^*	i-th particle velocity
St	Stokes number
Sr	Strouhal number
n_g	particle buoyancy force magnitude
n_{th}	prefactor of non-dimensional temperature gradient
n_l	lift proportionality factor
n_i	Brownian force
d	diameter
C_c	Cunningham correction factor
Kn	Knudsen number
C_s	thermal slip coefficient
C_m	momentum exchange coefficient
C_t	numerical factor
k_i	thermal conductivity for phase i
C_L	lift coefficient
Re	Reynolds number
Z_i	independent zero-mean Gaussian random number
k_B	Boltzman constant
v_s	settling velocity
k	kinetic energy
V	volume
v_d	deposition velocity
N	total number of particles
N_d	number of deposited particles
A_d	area of the wall for particle deposition
M_s	total deposited mass of particles
$\langle C \rangle$	bulk concentration of suspended particles
$\langle \cdot \rangle$	time-averaged value

Greek symbols

Δ	increment
ν	kinematic viscosity
α	thermal diffusivity
β	thermal expansion coefficient
ρ	density
δ_{ij}	Kronecker delta
ε_{ijk}	Levi-Civita symbol
ω	vorticity
λ	air free mean path
ε	kinetic energy dissipation
τ	temporal scale

Subscripts

vert	vertical
hor	horizontal
0	reference value
p	particle
f	fluid
s	scale
h	hot walls
c	cold walls
m	m-th cavity wall
l, r	left and right cavity walls
b, t	bottom and top cavity walls
q, d	front and back cavity walls

Superscript

$\widetilde{a}$	dimensional value
$\overline{a}$	volume-averaged value
$\widehat{a}$	wall-averaged value

vertical and horizontal wall Nusselt number (Nu) versus Ra in the range between 10^3 and 10^6. Danis et al. [15] used the Smoothed Particle Hydrodynamics (SPH) technique to investigate the natural convection in a squared 2D cavity over the same Ra number range. The obtained correlation were found to be in agreement with previous studies of the same flow configurations. The algebraic heat flux model proposed by Hanjalic and Vasic [16] was used to investigate the heat transfer in a 2D square cavity over the range $10^{10} \leqslant Ra \leqslant 10^{12}$. The reported Nusselt number for vertical and horizontal walls versus Rayleigh number were in relatively good agreement with the experiments carried out by Kirkpatrick and Bohn [17]. Using Direct Numerical Simulations (DNS), Fabregat and Pallares [18] investigated the heat transfer in a cubical Differentially Heated Cavity (DHC) for both laminar and turbulent regimes over the range $10^5 \leqslant Ra \leqslant 5.4 \times 10^8$ and reported correlations for the wall-averaged Nu on both the vertical and horizontal surfaces.

Regarding the transport of suspended material in fluids, the turbulent dispersion and wall deposition of airborne particles have attracted notable efforts due to their central role in the spreading of toxic or hazardous particulate matter in the environment [19], the fouling of active surfaces in heat exchange equipment [20], and recently, the transmission of infectious diseases including the COVID-19 [21]. When particles are small enough, the capacity of the turbulent air flow driven by thermal gradients to transport suspended particles and their likelihood to land on a solid surface strongly depends on the density ratio between the dispersed and carrier phases, the particle size and local characteristics of the background thermal and hydrodynamic fields. Puragliesi et al. [6] used DNS to investigate particle deposition in a 2D buoyancy-driven flow within a DHC at Ra numbers between 10^9 and 10^{10} using particles with diameters between 15 and 35 μm. Kalilainen et al. [22] experimentally studied the depletion dynamics of 1.0 and 2.5 μm particles inside a DHC at $Ra = 10^9$ with all walls insulated except the two opposing vertical walls that were kept at distinct temperatures. Dehbi et al. [23] used Large-Eddy Simulations (LES) to predict the air flow field and particle dynamics inside a DHC. The particle concentration was found to decay exponentially with time and the computed depletion rate constants were in very good agreement with experimental data for particles with diameters of 1.4 and 3.5 μm [22]. Kim et al. [24] extended the work of Kalilainen et al. [22] and Dehbi et al. [23] by using experiments and LES with wall-to-wall radiation effects and Lagrangian Particle Tracking (LPT). They reported excellent agreement between LES velocity and temperature fields and experimental data. Additionally, Kim et al. [24] investigated particle deposition velocity on thermally active walls providing data on the decay rates in a cubical cavity for different Rayleigh number and particle sizes. Lai et al. [25] investigated the role played by wall rugosity and concluded that the ratio of particle deposition rate on rough surfaces relative to smooth surfaces increased with the particle size and the velocity magnitude of the air flow. The effect of surface roughness was also investigated by Zhong

et al. [26] who reported that non-smooth walls enhanced the overall particle deposition.

Of particular interest is the work of Thatcher et al. [27] who experimentally determined the deposition rate of particles ranging from 0.1 to 2.5 μm onto smooth surfaces at $Ra = 5.4 \times 10^8$ and $Ra = 3.6 \times 10^9$. Using exactly the same flow set-up, Fabregat and Pallares [18,28,29] numerically investigated the hydrodynamics and particle deposition at $Ra = 5.4 \times 10^8$ using DNS coupled with a LPT approach. They proved that the numerical approach can satisfactorily predict the wall-averaged deposition rate and identified preferential deposition locations on the cavity walls.

By extending the analysis of Fabregat and Pallares [18] up to $Ra = 3.6 \times 10^9$, the present study has two goals, namely, (i) to assess the validity of the wall-averaged *Nu* correlation over the range $10^7 \leqslant Ra \leqslant 5.4 \times 10^8$ up to this Rayleigh number, and (ii) to compare the numerical results of wall-average particle deposition rate with the experiments reported by Thatcher et al. [27] and the boundary layer solutions presented in Pallares and Fabregat [28].

The paper is organized as follows: Section 2 contains a description of the physical and mathematical models with details of the computational domain and initial and boundary conditions. In Section 3 we present the hydrodynamics results and discuss the updated correlation between *Nu* vs *Ra* in the context of previous studies. Spatial distribution of the particle deposition and the average deposition rate on each thermally active wall for each particle size are also presented. Section 4 analyzes the comparison of the numerical predictions with experiments and boundary layer theory. Finally, in Section 5 we outline the conclusions and comment on future work.

2. Physical and mathematical model

Following the experimental set-up used by Thatcher et al. [27], the computational domain used here consists in a cubical cavity of side length $\widetilde{l} = 3.14$ m filled with air where two pairs of opposed walls are kept at constant but different temperatures. Note that dimensional quantities are denoted with a tilde. The turbulent flow is driven by holding the bottom (*floor*) and left vertical wall temperature constant at $\widetilde{T}_h$, i.e. $\widetilde{T}(\widetilde{x}, -\widetilde{l}/2, \widetilde{z}) = \widetilde{T}(-\widetilde{l}/2, \widetilde{y}, \widetilde{z}) = \widetilde{T}_h$ (in red in Fig. 1) and the top (*ceiling*) and right vertical walls at $\widetilde{T}_c = \widetilde{T_h} - 1.3$ K, i.e. $\widetilde{T}(\widetilde{x}, \widetilde{l}/2, \widetilde{z}) = T(\widetilde{l}/2, \widetilde{y}, \widetilde{z}) = \widetilde{T}_c$ (in blue in Fig. 1). The two remaining walls, normal to direction z, are assumed perfectly insulated, i.e.

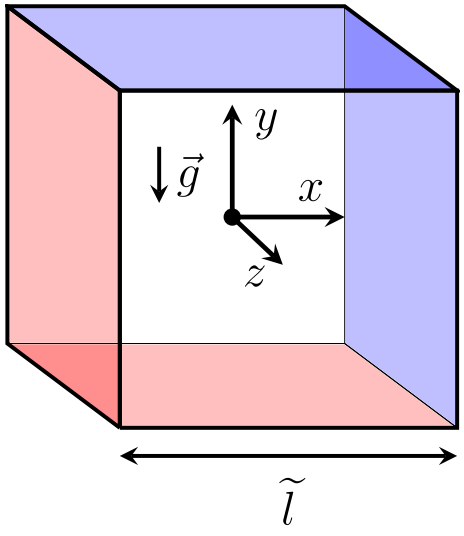

Fig. 1. Sketch of the computational domain.

$$\left.\frac{\partial \widetilde{T}}{\partial \widetilde{z}}\right|_{\widetilde{z}=\pm\widetilde{l}/2} = 0.$$

All physical properties of both the carrier (air) and dispersed phases are evaluated at the reference temperature $\widetilde{T}_0 = (\widetilde{T}_h + \widetilde{T}_c)/2 = 300$ K and gravity is aligned with the $-y$ direction.

To investigate the transport and deposition of suspended material on each surface, 55,000 particles of 0.1, 0.5, 0.7, 1.3 and 2.5 μm in diameter were randomly seeded within the domain once statistically steady conditions were reached. The total of 275,000 idealized (smooth and spherical) particles were allowed to circulate within the cavity over $\Delta\widetilde{t} = 1.4 \times 10^3$ s. Using identical flow computational set-up and mathematical models as in Fabregat et al. [18] (see this reference for details), here we use the Boussinesq approximation assuming incompressibility and neglecting radiation and viscous dissipation. Thus, the non-dimensional mass, momentum and heat conservation equations can be written as:

$$\frac{\partial u_i}{\partial x_i} = 0 \tag{1}$$

$$\frac{\partial u_i}{\partial t} + u_j\frac{\partial u_i}{\partial x_j} = -\frac{\partial p}{\partial x_i} + \frac{Pr}{\sqrt{Ra}}\frac{\partial^2 u_i}{\partial x_j \partial x_j} + PrT\delta_{i2} \tag{2}$$

$$\frac{\partial T}{\partial t} + u_j\frac{\partial T}{\partial x_j} = \frac{1}{\sqrt{Ra}}\frac{\partial^2 T}{\partial x_j \partial x_j} \tag{3}$$

where t is time, u_i is the velocity component in the direction x_i, p is pressure, T is temperature perturbation and *Ra* and *Pr* are the Rayleigh and Prandtl groups defined as:

$$Ra = \frac{g\beta T_s \widetilde{l}_s^3}{\nu\alpha} = 3.6 \times 10^9 \tag{4}$$

$$Pr = \frac{\nu}{\alpha} = 0.7. \tag{5}$$

where ν is the kinematic viscosity, α is the thermal diffusivity, β is the thermal expansion coefficient and g is the gravitational acceleration. The length, velocity, time and temperature scales are $l_s = \widetilde{l} = 3.14$ m, $u_s = \alpha Ra^{1/2}/\widetilde{l} = 0.428$ m s^{-1}, $t_s = \widetilde{l}/u_s = 7.34$ s and $T_s = \Delta\widetilde{T} = 1.3$ K respectively.

Note that the equation of state that relates fluid density ρ_f and temperature deviation under the Boussinesq approximation can be written as:

$$\rho_f = \rho_0\left[1 - \beta\left(\widetilde{T} - \widetilde{T}_0\right)\right] \tag{6}$$

where ρ_0 is the reference density at $\widetilde{T}_0$. Eqs. (1)–(3) along with the initial and boundary conditions are solved using Nek5000 [30], an open source, high-order spectral element method (SEM) based solver for the incompressible Navier–Stokes equations. The basis functions in SEM are Nth-order tensor-product Lagrange polynomials on the Gauss–Lobatto–Legendre quadrature points inside each element that ensure fast evaluation and low storage cost operators [31]. Nek5000 uses a semi-implicit kth-order Backward Difference Formula (BDFk) and kth-order Extrapolation (EXTk) timestepping in which the time derivative is approximated by a BDFk while the nonlinear terms (and other forcings) are treated with a EXTk. The viscous and pressure terms are treated implicitly. This approach leads to a linear unsteady Stokes problem to be solved at each time step, which comprises a Helmholtz equation for each component of velocity (and temperature or scalars) and a Poisson equation for pressure [32]. Nek5000 has been extensively used to carry out both DNS and LES simulations in a wide variety of flow configurations and applications [33–35].

The mesh grid, with a total of approximately 300 million nodes,

ensures the explicit resolution of all spatial and temporal scales according to the resolution criteria proposed by Scheel et al. [36] for similar buoyancy driven flow configurations. The minimum and maximum grid grid spacings are $\Delta X_{min} = \Delta Y_{min} = \Delta Z_{min} = 3.3 \times 10^{-3}$ and $\Delta X_{max} = \Delta Y_{max} = \Delta Z_{max} = 1.4 \times 10^{-4}$ non-dimensional units, respectively. Further details on numerics and mesh generation can be found in Fabregat and Pallares [18].

Regarding the transport of the dispersed phase, the equation of motion of an idealized spherical and smooth particle can be derived from the force balance acting upon it (see Fabregat and Pallares [18] for details). Thus, the position of a given particle x_i^* can be written as:

$$\frac{dx_i^*}{dt} = u_i^* \tag{7}$$

where the particle velocity u_i^* can be determined as:

$$\frac{du_i^*}{dt} = \underbrace{\frac{u_i - u_i^*}{St_p}}_{\text{Drag}} + \underbrace{n_g \delta_{i2}}_{\text{Buoyancy}} + \underbrace{n_{th}\frac{\partial T}{\partial x_i}}_{\text{Thermophoresis}} + \underbrace{n_l \varepsilon_{ijk}\left[u_j^* - u_j\right]\omega_k}_{\text{Lift}} + \underbrace{n_i(t)}_{\text{Brownian}} \tag{8}$$

where St_p is particle the Stokes number, n_g is the magnitude of the buoyancy force experienced by a particle, δ_{ij} is the Kronecker delta, n_{th} is the pre-factor of the non-dimensional temperature gradient, n_l is the lift proportionality factor, ε is the Levi–Civita symbol, $\vec{\omega} = \vec{\nabla} \times \vec{u}$ is the flow vorticity and n_i is the Brownian force.

The particle transport model presented in Eqs. (7) and (8) assumes that there are five relevant forces acting on the particle, namely, hydrodynamic drag and lift, buoyancy, thermophoresis and Brownian. Under the one-way coupling approach, used in this work, the dispersed phase is assumed to have negligible contributions to the carrier phase momentum conservation. This assumption is valid for small enough particles and dilute systems.

2.1. Drag

Hydrodynamic drag accounts for the fluid resistance or friction a particle experiences as it moves with respect to the carrier phase. The hydrodynamic drag can be characterized by the particle Stokes number defined as the ratio of the particle and flow characteristic times. Small St_p are associated to particles that rapidly react to changes in accelerations in the underlying flow while large Stokes are found in inertia-dominated particles. The Stokes number for a particle of diameter $\widetilde{d}_p$ can be written as:

$$St_p = \frac{d_p^2}{18 C_c}\frac{\rho_p}{\mu_f} u_s l_s \tag{9}$$

where ρ_p is the particle density, C_c is the Cunningham correction factor.

$$Kn = \frac{2\lambda}{\widetilde{d}_p} \tag{10}$$

$$C_c = 1 + Kn\left[1.205 e^{-0.0026/Kn} + 0.425 e^{-0.7400/Kn}\right] \tag{11}$$

where $d_p = \widetilde{d}_p / l_s$ is the non-dimensional particle diameter and $\lambda = 6.8 \times 10^{-8}$ m is the free mean path in air at $\widetilde{T}_0$ [37].

2.2. Buoyancy (weight)

The magnitude of the buoyancy force experienced by a particle within a fluid with different density under a gravitational field with acceleration magnitude $g = 9.81$ m s^{-2} can be written as:

$$n_g = -g\left(1 - \frac{\rho_f}{\rho_p}\right)\frac{l_s}{u_s^2}. \tag{12}$$

2.3. Thermophoresis

Thermophoresis is the force due to gradients in the temperature field across the particle characteristic length. The pre-factor of the non-dimensional temperature gradient, n_{th}, is defined as [38]:

$$n_{th} = -18\frac{K_{tp}}{d_p^2}\frac{\nu_f^2}{\widetilde{T}_0}\frac{\rho_f}{\rho_p}\frac{T_s}{l_s^2 u_s^2} \tag{13}$$

where the factor K_{tp}, defined as,

$$K_{tp} = \frac{2C_s\left(k_f + 2k_p Kn\right)\left[1 + 2Kn(1.2 + 0.41\exp(-0.44/Kn))\right]}{(1 + 6C_m Kn)\left(2k_f + k_p + 4k_p C_t Kn\right)}, \tag{14}$$

contains three constant set to $C_s = 1.17, C_m = 1.14$ and $C_t = 2.18$. Note that the negative sign in n_{th} indicates that the force points in the direction of maximal temperature decay.

2.4. Lift

The hydrodynamic force acts perpendicular to the flow direction and is proportional to the cross product of the velocity difference between the two phases and the local vorticity in the carrier phase. The proportionality factor has the form

$$n_l = C_L\frac{\rho_f}{\rho_p} \tag{15}$$

where the lift coefficient C_L is defined as [39]:

$$C_L = \left[5.816\sqrt{\frac{Sr_p}{2Re_p}} - 0.875\frac{Sr_p}{2}\right]\frac{3}{4Sr_p}\frac{J(\varepsilon)}{2.255} \tag{16}$$

where the particle Reynolds number is Re_p, particle Strouhal number is Sr_p, ε and J are determined using the relations:

$$Re_p = \left|u_i^* - u_i\right| d_p Re, \tag{17}$$

$$Sr_p = \frac{\left|\epsilon_{ijk}\left[u_j^* - u_j\right]\omega_k\right|}{\left|u_j^* - u_j\right|^2} d_p, \tag{18}$$

$$\varepsilon = \sqrt{\frac{Sr_p}{Re_p}}, \tag{19}$$

$$J(\varepsilon) = 0.6765\{1 + \tanh[2.5\log_{10}(\varepsilon + 0.191)]\}\{0.677 + \tanh[6(\varepsilon - 0.32)]\}. \tag{20}$$

2.5. Brownian

For small enough particles, the net force due to molecular vibrations may not be negligible and, therefore, contribute to the transport. This Browninan force takes the form [40]:

$$n_i\left(t\right) = Z_i\sqrt{\frac{2\pi}{\Delta t}216\frac{\rho_f}{\rho_p^2}\frac{k_B\widetilde{T}_0\nu_f}{d_p^5\pi^2 C_c}\frac{\widetilde{t}^3}{\widetilde{l}^7}} \tag{21}$$

where Z_i is independent zero-mean Gaussian random number, $k_B = 1.38064852 \times 10^{-23}$ J K^{-1} is the Boltzmann constant.

2.6. Settling velocity

To gain insight into the role played by the flow hydrodinamics on the wall deposition, the deposition rate is often compared with the settling velocity, v_s. This quantity is determined by assuming that the only forces acting on a particle suspended in a quiescent fluid are drag and buoy-

ancy. Simplifying Eq. (8), the expression for v_s yields

$$v_s = St_p n_g \delta_{i2}. \tag{22}$$

2.7. Exponential-Lagrangian Tracking Schemes

Eqs. (7) and (8) are temporally integrated using Exponential-Lagrangian Tracking Schemes (ELTS) [41]. ELTS are inherently stable and offer, at least, $\mathcal{O}(\Delta t^2)$ local truncation errors depending on the application. Details on the ELTS temporal discretization can be found in [18].

The Spectral Element Method (SEM) spatial discretization used in Nek5000 where the numerical approximation in each element can be expressed as a three-dimensional Legendre polynomial expansion of order N^3 is used to interpolate the particle velocity on the previous time step or in any other intermediate time in the predictor–corrector approach used in ELTS (see details in [18]).

3. Results

3.1. Flow hydrodynamics

To illustrate the hydrodynamic and thermal fields under statistically developed conditions, Fig. 2 shows three slices for an arbitrary flow snapshot at $t \approx 200$ as indicated in panel (a). The instantaneous non-dimensional temperature field (T) at $z = 0$ in panel (b) clearly shows the signature of the persistent large scale clockwise recirculation rising along the hot vertical wall and descending along the cold one. The distinct levels of turbulence intensities between the boundary layers along the solid surfaces and the mildly fluctuating central region clearly emerge in the temperature field characterized by the presence of turbulent intrusions in the vicinity of walls. To elucidate the rich flow structure within the boundary layers, panel (c) shows the horizontal velocity component u_x very close to the top cold wall ($y = 0.495$). The fine scale turbulence structure is characterized by the presence of streak-like patterns within the momentum boundary layer mostly aligned with the dominant current direction. When compared to panel (c), the vertical velocity component u_y near the vertical cold wall at $x = 0.495$ shown in panel (d) exhibits a distinct structure that reflects the difference between both walls orientation with respect to the gravitational action.

To illustrate the temporal evolution of the flow under statistically converged conditions Fig. 3 shows a sample of the time evolution of the volume-averaged (indicated with an overbar) kinetic energy k and its dissipation ε defined as:

$$\overline{k} = \frac{1}{2V}\int_V \left(u_i u_i\right) dV \tag{23}$$

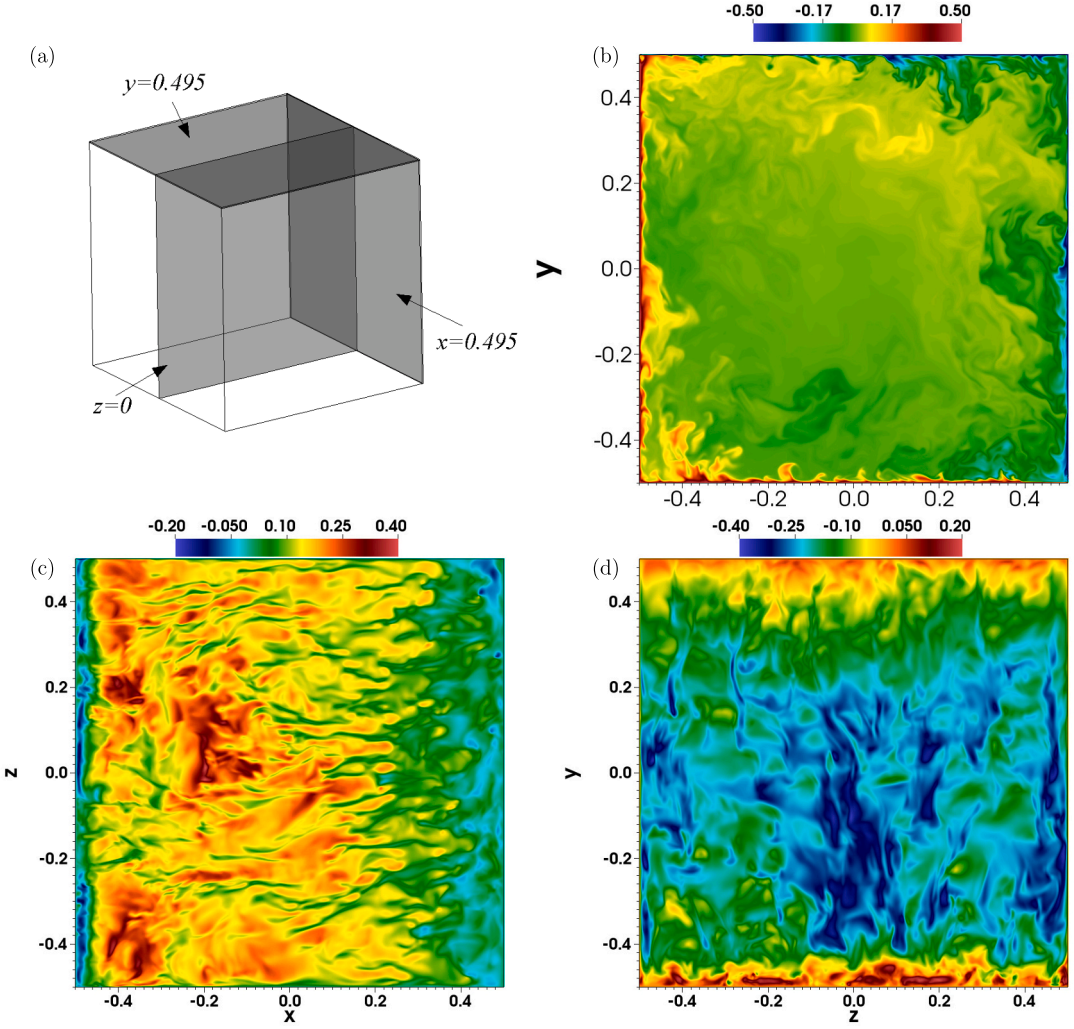

Fig. 2. (a) Three slices across the cavity domain: (b) instantaneous temperature field at $z = 0$, (c) horizontal velocity component at $y = 0.495$ and (d) vertical velocity component at $x = 0.495$.

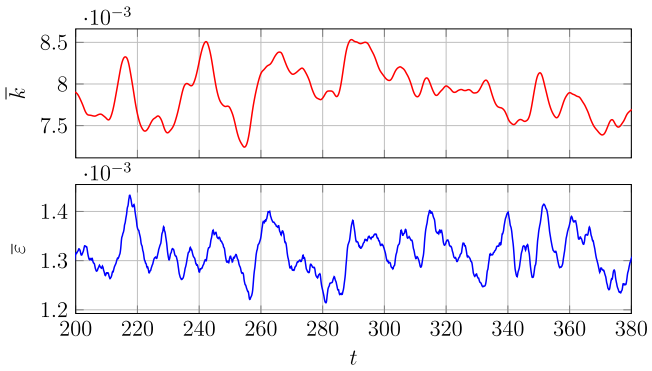

Fig. 3. History sample showing the temporal evolution of the volume-averaged turbulent kinetic energy $\bar{k}$ (top panel) and turbulent dissipation $\bar{\varepsilon}$ (bottom).

and

$$\bar{\varepsilon} = \frac{Pr}{\sqrt{Ra}V}\int_V \left(\frac{\partial u_i}{\partial x_i}\frac{\partial u_i}{\partial x_i}\right) dV \tag{24}$$

where V is cavity volume. The corresponding non-dimensional temporal scale is $\tau = \langle\bar{k}\rangle/\langle\bar{\varepsilon}\rangle \approx 6$ where angle brackets indicate temporally averaged quantities.

Fig. 4 shows the time-averaged non-dimensional horizontal (a) and vertical (b) velocity components (u_x, u_y) at $z = 0$. It can be seen that the contours are antisymmetrical with respect to the origin of the coordinate system located at the center of the cavity (see Fig. 1). The corresponding profiles of the non-dimensional time-averaged temperature and velocity components u and v along the vertical and horizontal cavity bisectors are shown in Fig. 5. Panel (a) shows the temperature results for the present $Ra = 3.6 \times 10^9$ in black. For comparison, the profiles at $Ra = 10^7$ (red), 10^8 (blue) and 5.4×10^8 (green) presented in Fabregat and Pallarès [18] are also included. Analogously, panel (b) shows the time-averaged profiles of u along the vertical cavity bisector and v along the horizontal one. These results show the progressive thinning of both the momentum and thermal boundary layers and the increase of wall heat transfer and wall shear stress as Rayleigh number increases. It can also be seen that vertical velocity near the hot and cold walls is slightly higher than the horizontal velocity near the hot floor and cold ceiling.

The temporal evolution of $\widehat{Nu}$ is shown in Fig. 6 over the same temporal sample used in Fig. 3. Hot and cold vertical walls results are shown in orange and teal, respectively, while red and blue are used for the hot and cold horizontal walls. Temporal averages of wall-averaged Nusselt number for the horizontal and vertical walls are

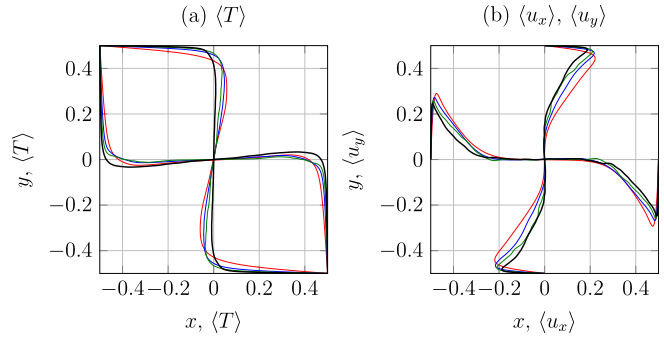

Fig. 5. Time-averaged non-dimensional temperature (a) and velocity (b) profiles along the horizontal and vertical bisectors of the symmetry plane of the cavity z $= 0$. Red, blue, green and black represents $Ra = 1.0 \times 10^7, Ra = 1.0 \times 10^8, Ra = 5.4 \times 10^8$ and $Ra = 3.6 \times 10^9$ respectively.

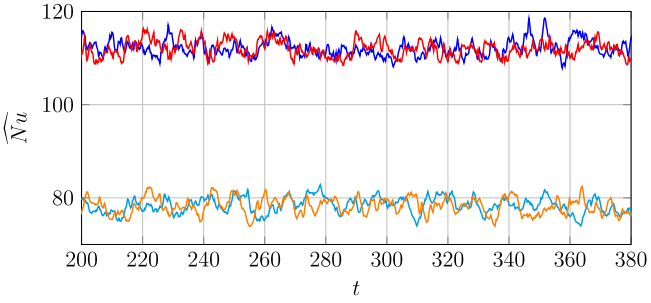

Fig. 6. Temporal evolution of the (absolute) wall-averaged Nusselt number on each wall. Red and blue correspond to the horizontal hot and cold walls respectively while orange and teal correspond to the vertical hot and cold walls.

approximately $\langle\widehat{Nu}_b\rangle = \langle\widehat{Nu}_t\rangle = 112$ and $\langle\widehat{Nu}_l\rangle = \langle\widehat{Nu}_r\rangle = 78$, respectively. Where average heat flux across a given wall is defined as $\widehat{Nu}_m$:

$$\widehat{Nu}_m = -\int_{\Omega_m} \frac{\partial T_m}{\partial n_m}\, d\Omega_m \tag{25}$$

where $m = \{b, t, l, r, f, q\}$ represent each face of the cubical domain and n_m represent the corresponding face-normal direction. By definition, $\widehat{Nu}_f = \widehat{Nu}_q = 0$ on the adiabatic walls.

Fig. 7 shows the dependence of the temporal and wall-averaged Nusselt number on the Rayleigh number over the range between 10^3

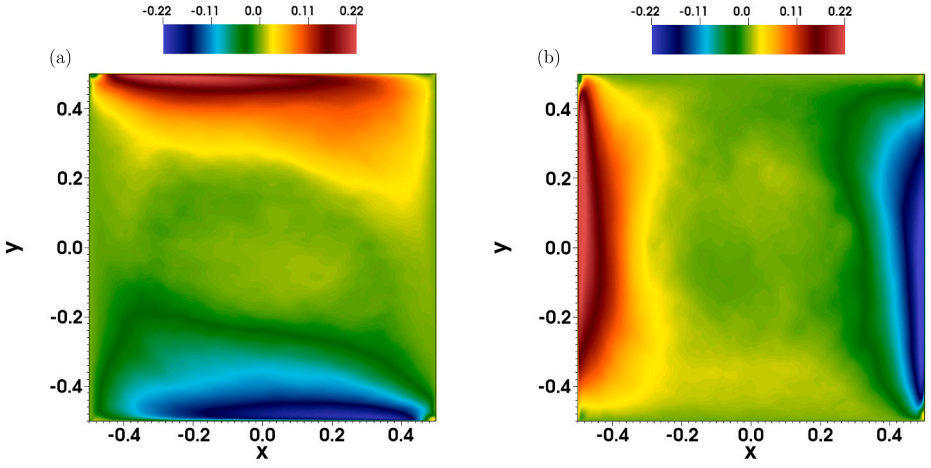

Fig. 4. Time-averaged non dimensional horizontal velocity (a) and vertical velocity (b) components at $z = 0$.

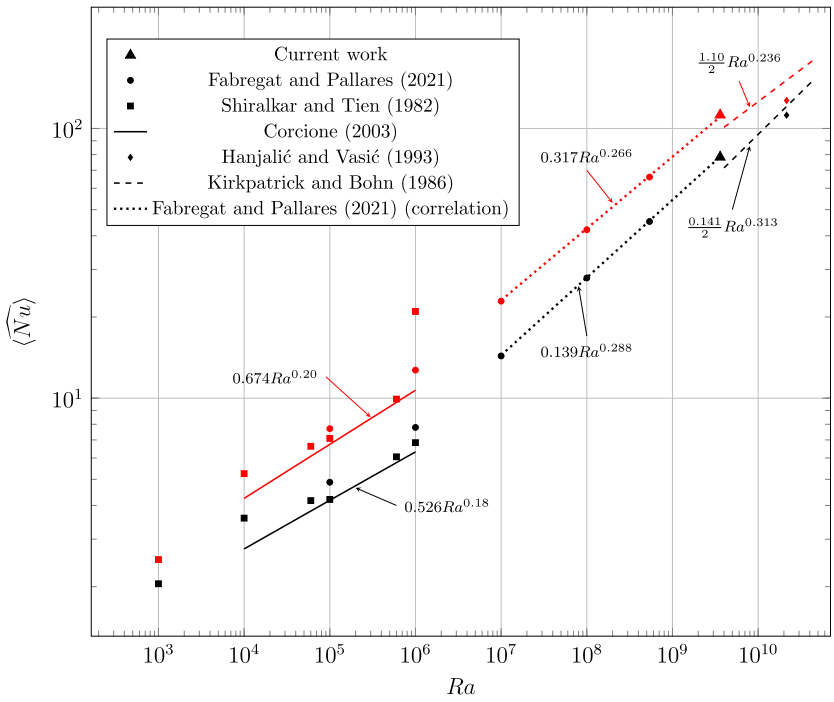

Fig. 7. Dependence of the vertical (black) and horizontal (red) time and wall-averaged Nusselt number on the Rayleigh number. Corcione [14] and Kirkpatrick & Bohn [17] correlations are show as solid and dashed lines respectively. Dotted line indicates the correlation for the current results over the entire Rayleigh number range.

and 10^{11} using black and red for the vertical and horizontal wall respectively. Results include 2D numerical simulations [12,14], 3D Reynolds-Averaged Navier–Stokes (RANS) solutions [16] and experiments [17]. The present DNS results at $Ra = 3.6 \times 10^9$, shown using triangles, suggest that the correlation derived for $10^7 \leqslant Ra \leqslant 5.4 \times 10^8$ by Fabregat and Pallarès [18] can be extended up to $Ra = 3.6 \times 10^9$. Specifically, these correlations for both the horizontal and vertical wall-averaged Nusselt number over the $10^7 \leqslant Ra \leqslant 3.6 \times 10^9$ are:

$$\langle \widehat{Nu} \rangle_{vert} = 0.139 Ra^{0.288}, \tag{26}$$

$$\langle \widehat{Nu} \rangle_{hor} = 0.317 Ra^{0.266} \tag{27}$$

In comparison to the correlations in [17] estimated from experimental data, the present correlations in Eqs. (26) and (27) predict slightly higher wall-averaged Nusselt number on both wall orientations. The extrapolation of the present correlations and those reported in [17] up to $Ra = 3.6 \times 10^9$ predicts larger values of wall-averaged Nusselt number in comparison to those reported by Hanjalić and Vasić [16].

3.2. Particle dynamics and deposition

To investigate the particle deposition on thermally active walls, a total of 275,000 ideal solid spherical particles of 0.1, 0.5, 0.7, 1.3 and 2.5 μm in diameter were randomly seeded and advected according to the model in Eqs. (7) and (8). Following the same approach used in Fabregat and Pallares [29], once the flow reached statistically steady conditions, the particle trajectory and deposition locations on each wall over the next $\Delta t = 180$ time units were recorded. The particle was assumed to deposit on the corresponding wall when the distance between the center of a particle and a wall was equal or less than its radius. No rebound and resuspension have been considered. Deposited particles are randomly reseeded within the cavity domain to ensure a constant number of suspended particles across the entire simulation. The Stokes number of the smallest and the biggest particles are $St_p = 8.4 \times 10^{-9}$ and $St_p = 3.3 \times 10^{-5}$ respectively. The ability of the model in Eqs. (7) and (8) to predict the rate at which particles deposit on each surface of the cavity at $Ra = 3.6 \times 10^9$ is assessed by comparing the numerical results with the experiments of Thatcher et al. [27] and also with the predictions from the Boundary Layer (BL) model derived by Pallares and Fabregat [28].

Figs. 8–12 show the landing positions on each wall for each particle size using red, blue and black markers to distinguish between hot, cold and adiabatic walls respectively. Arrows are used to indicate the large scale flow direction.

The absence of deposition for particles of 0.1 and 0.5 μm in diameter suggests that thermophoresis force prevents the smallest particles from landing on the hot walls.

While landing positions across the vertical cold wall are approximately homogeneous, the horizontal wall exhibits larger impact density near the region where the ascending fluid along the vertical hot wall impinges on the ceiling. This can be explained by the intensified favourable temperature gradient in the vicinity of this corner where a hot vertical wall meets a cold horizontal one. On the adiabatic walls, where no thermal forcing hinders or favors particle transport by means of thermophoresis, only a few particle depositions were recorded.

For larger particles of 0.7 μm, results in Fig. 10 suggest that deposition on the ceiling are restricted to the region where the (negative) vertical gradient of temperature exceeds the gravitational force with most of landings occurring within $-1/2 < x < -1/3$. Similar magnitudes between these two opposing terms explain also the few depositions recorded on the hot horizontal wall. Again, the absence of thermal and gravitational components along the z-axis results in a few landings on the adiabatic walls.

As shown in Figs. 11 and 12, as particle size increases, the contribution of gravity to particle transport relative to thermophoresis increases. Thus, while deposition rate increases at the hot floor surface, it decays at the cold ceiling. Despite this, the intensified thermal gradient near the bottom right corner where descending cold fluid impinges on the hot floor leads to decreased floor deposition rate for particles of 1.3 μm in the vicinity of this location. This inhomogeneity vanishes in the case of the largest particles as shown in Fig. 12. Note that Fig. 11 has one deposited particle on the cold ceiling and this particle is not taken into

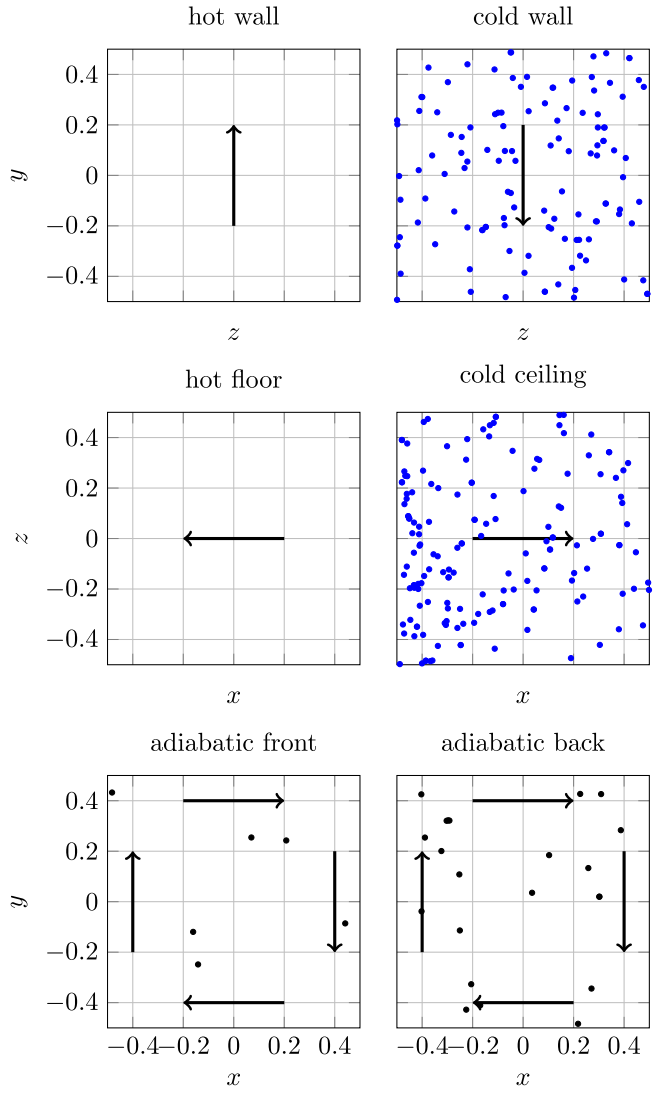

Fig. 8. Landing positions on the walls of particles with $\widetilde{d}_p = 0.1$ μm. The direction of the large scale circulation close to the wall is indicated with an arrow.

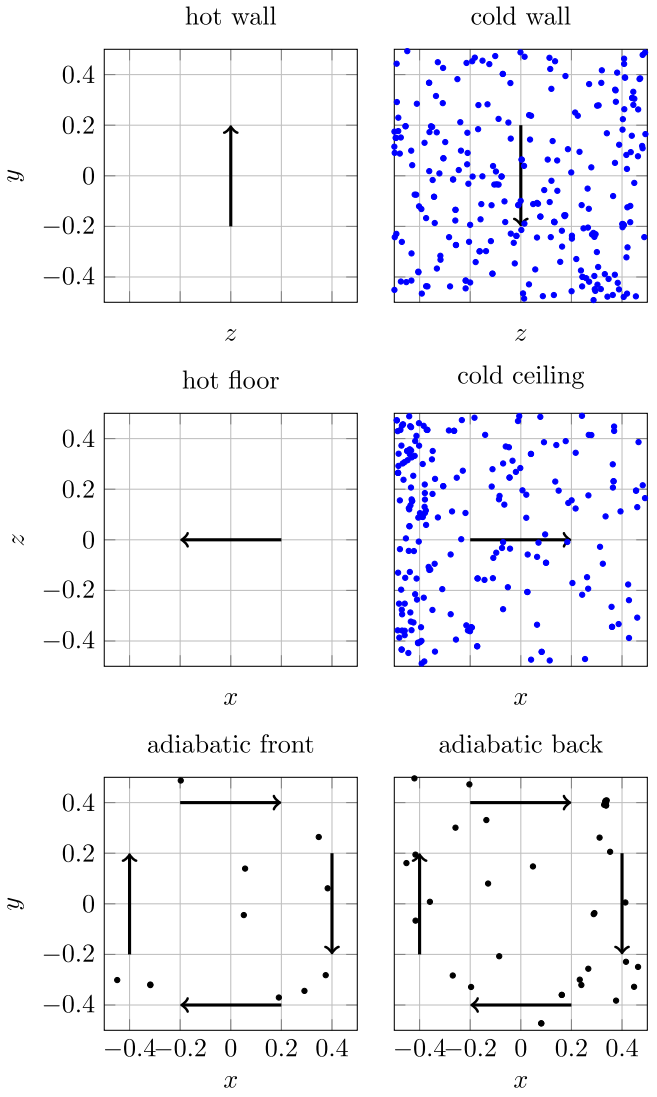

Fig. 9. Landing positions on the walls of particles with $\widetilde{d}_p = 0.5$ μm. The direction of the large scale circulation close to the wall is indicated with an arrow.

account when calculating the deposition velocity.

The results for particles with diameters of 1.3 and 2.5 μm suggest that although thermophoresis forces are no longer able to establish a net transport of particles towards the ceiling, they remain significant in the horizontal direction as evidenced by the deposition solely on the cold vertical wall. Deposition on thermally inactive walls are found to be mostly independent of the particle size over the considered diameter range.

The wall-averaged deposition velocity is defined as:

$$\widehat{v}_d = \frac{\widetilde{M}_s}{\Delta\widetilde{t}_d \left\langle C \right\rangle \widetilde{A}_d} = \frac{N_d}{N} \frac{\widetilde{l}}{\Delta\widetilde{t}_d} \tag{28}$$

where N is the total number of particles, N_d is the number of deposited particles over the time span $\Delta\widetilde{t}_d$ and area $\widetilde{A}_d = \widetilde{l}^2$, $\widetilde{M}_s = \rho_p \widetilde{A}_d \widetilde{V}_p$ is the total deposited mass of the particles, $\widetilde{V}_p = (\pi/6)\widetilde{d}_p^3$ is the particle volume and $\langle C \rangle = \rho_p N \widetilde{V}_p / \widetilde{l}^3$ is the bulk concentration of suspended particles which is kept constant in the simulations. Fig. 13 shows the dimensional deposition velocity along the perimeter of the vertical symmetry plane of the cavity. The present DNS wall-averaged deposition velocity for each particle size and thermally active wall are shown in Fig. 13 as horizontal dark blue lines. Using empty and filled black markers for the two different reported experiments at $Ra = 3.6 \times 10^9$, the same figure also shows the experimental results by Thatcher et al. [27] along with the experimental detection limit depicted using a red dashed line. BL model predictions of wall-averaged deposition velocity from Pallares and Fabregat [28] are shown in magenta color. Green dashed line shows settling velocity defined in Eq. (22). For completeness, we also included using teal lines the results by Kim et al. [24], who numerically simulated a DHC with one pair of vertical thermally active walls using LES at $Ra = 10^9$ to determine the deposition rate of 0.7, 1.3 and 2.5 μm particles on the thermally active vertical walls and 0.7 μm particles on the adiabatic floor.

DNS and BL model predictions of the deposition rate on both cold walls for the smallest particles of 0.1 and 0.5 μm are in a good agreement. When compared to experiments of Thatcher et al. [27], both DNS and BL model underpredict the rate of deposition of 0.1 μm particles on both cold walls while slightly overpredicted values are found for 0.5 μm particles. For these two particle sizes, DNS predicts no deposition on the hot walls while BL model are found to predict relatively small rates in quite good agreement with the experimental results. In the case of particles with diameter 0.1 μm, experimental results are in between the

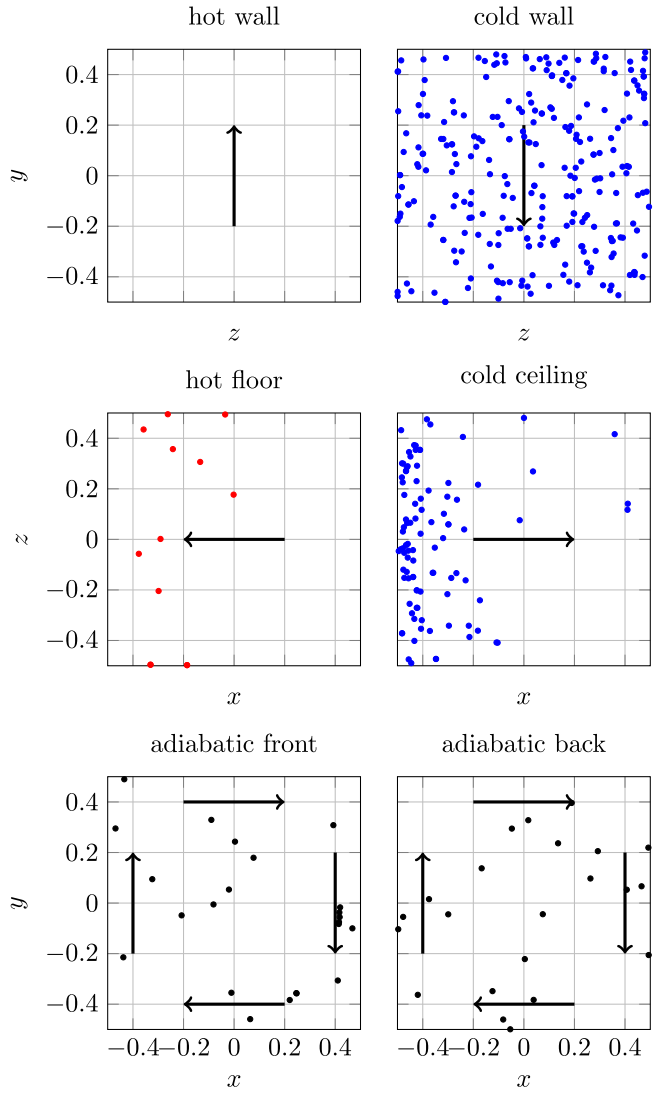

Fig. 10. Landing positions on the walls of particles with $\widetilde{d}_p = 0.7$ µm. The direction of the large scale circulation close to the wall is indicated with an arrow.

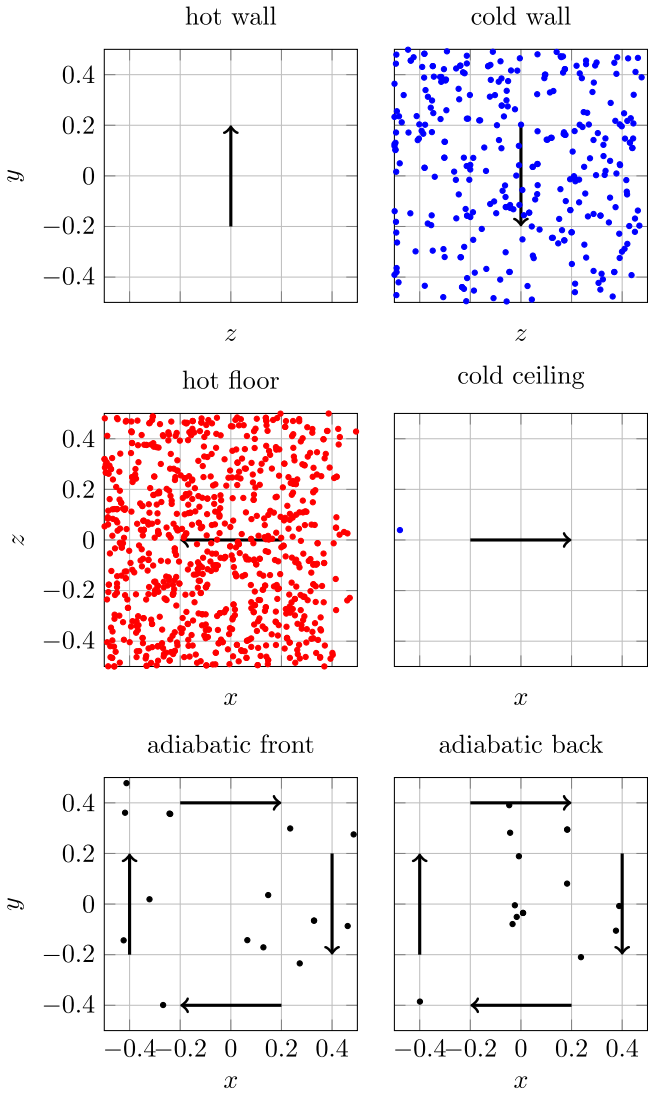

Fig. 11. Landing positions on the walls of particles with $\widetilde{d}_p = 1.3$ µm. The direction of the large scale circulation close to the wall is indicated with an arrow.

BL model prediction and the settling velocity. Experimental values for particles of 0.5 µm are notably smaller that those obtained by the BL model which are in very good agreement with the settling velocity. BL model also predict a very small deposition rate on the vertical wall for 0.1 µm but no deposition for 0.5 µm particles. Experimental data on this vertical surface is below (0.1 µm) or very close (0.5 µm) to the detection limit.

For particles of 0.7 µm, experimental deposition rates on the hot floor are bounded between the BL and the numerical predictions. Although neither BL nor DNS predict any deposition on the vertical hot wall, measurements of Thatcher et al. [27] did record some particle deposition, albeit, very close to the detection level. Although exhibiting a fair amount of data dispersion, experimental deposition rate on the cold ceiling is in good agreement with DNS results (BL model predict no deposition). The significant value of deposition rate on this surface suggests that the vertical thermophoretic force is capable of balancing the gravitational force along the vertical direction. All three predictions, DNS, BL model and experiments exhibit very good agreement on the cold vertical wall.

Current DNS, BL model and experimental results are in very good agreement for the largest particles of 1.3 and 2.5 µm in diameter. Both the numerical simulations and the BL solutions predict particles exclusively depositing on the floor and on the right cold wall with no impacts on the left warm wall and cold ceiling. In contrast, experimental results reported a few depositions on these two surfaces although data is notably dispersed and near the detection limit. Despite differences in the flow configuration, the values of deposition velocity reported by Kim et al. [24] for $Ra = 10^9$ are quite similar.

4. Discussion

There exists a discrepancy between the DNS deposition rate predictions and the values obtained with the BL model and the experimental measurements for the particles between 0.1 and 0.7 µm. Specifically, while DNS predicted no deposition for the 0.1 and 0.5 µm particles on the hot floor, BL models results were in agreement to the experiments which reported non-negligible deposition rates above the detection level (see Fig. 13). Similarly, DNS for the 0.7 µm particles under-predicted the experimental observations on the same surface. These differences might be explained, first, by the construction of the BL solutions. In the derivation of the particle deposition rate (see [28]), the dispersed phase velocity was decomposed into two components, one

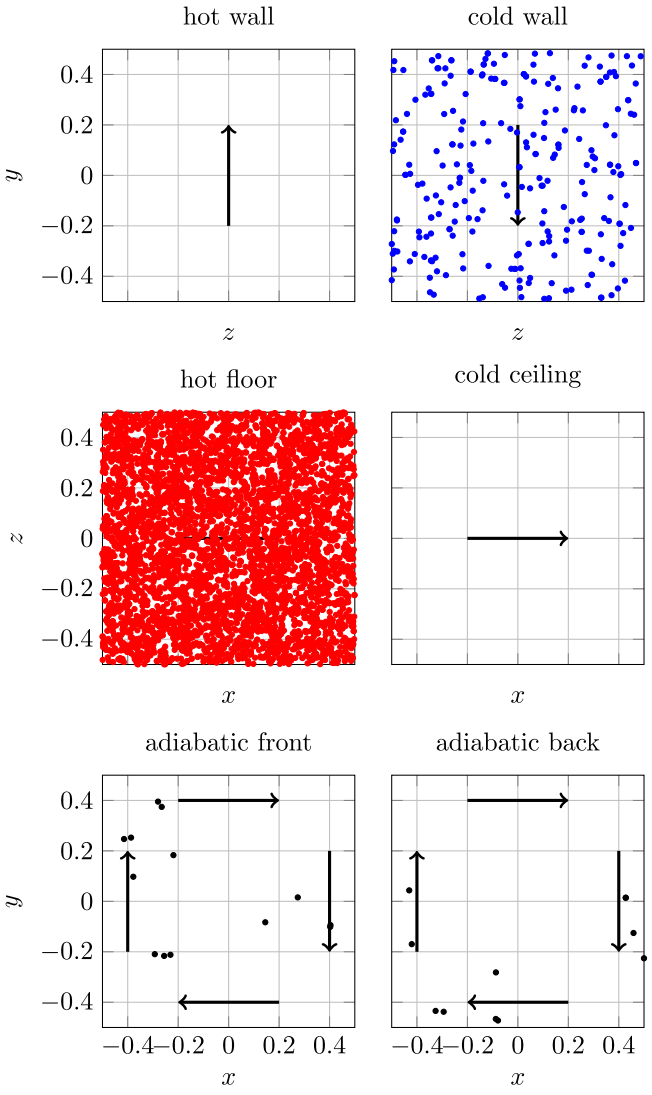

Fig. 12. Landing positions on the walls of particles with $\widetilde{d}_p = 2.5\,\mu m$. The direction of the large scale circulation close to the wall is indicated with an arrow.

accounting for gravitational settling velocity and the other accounting for the rest of the transport contributions, namely, hydrodynamic drag, thermophoresis and Brownian forces. By doing so, the form of the force balance without the gravitational contribution could be integrated and then corrected to account for this initially neglected term. As shown in Pallares and Fabregat [28], these approaches are capable of accurately predicting both DNS and experiments for both 0.1 and 0.5 μm in a $Ra = 5.4 \times 10^8$ cavity. However, when the magnitude of the thermophoresis effect is comparable or larger than gravity (this is when particles are small and Ra is high), these models tend to over-predict the deposition on horizontal walls as a result of the correction to take into account the gravity force. Thereby, under conditions dominated by thermophoresis, BL model tend to predict deposition velocities close to the settling velocity (See Fig. 13 for particles of 0.1, 0.5 and 0.7 μm). To illustrate the relative importance of the gravitational and thermophoresis forces, Table 1 shows the non-dimensional values of the buoyancy (n_g) and the surface averaged thermophoresis terms ($n_{th}\frac{dT}{dy}$) on the horizontal walls for each particle size. For comparison, the surface horizontal thermophoresis term ($n_{th}\frac{dT}{dx}$) on the thermally active vertical walls has also been included. All in all, in the absence of gravitational effects, the BL models predictions on vertical walls are in good agreement with DNS and experimental results (See Fig. 13).

Notably, Thatcher et al. [27] mention that their experimental results do not agree with the theoretical predictions of Nazaroff and Cass [42] for some particle sizes. This observation could suggest that the balance between thermophoresis and gravitational effects may not be properly accounted for in this model. In addition, the experimental non-negligible deposition rate reported by Thatcher et al. [27] might be explained by enhanced gravitational effects associated to particle agglomeration. In this regard, Kim et al. [24] used experiments to investigate particle removal rates in a DHC of side length 0.7 m with two opposite vertical walls held at different temperatures and the rest adiabatic. The transport of monodisperse particles with aerodynamically equivalent diameters of 0.7, 1.4, and 3.5 μm, which corresponds to 0.5, 1.0 and 2.5 μm physical diameter, at $Ra = 10^9$ was estimated by sampling particle concentration every 10 to 30 min for 1.0 and 2.5 μm and 1 h for 0.5 μm particles. Using microscopic imaging, these authors reported the existence of duplets, triplets and even quadruplets produced by particle adhesion phenomenon. Table 2 shows the Kim et al. [24] average and standard deviation results for single and agglomerate fractions from the particle size also considered in the present work. Using the same experimental setup and similar flow conditions, Kalilainen et al. [22] reported single particle fractions of between 69% and 74% and between 89% and 95% for 1.0 and 2.5 μm respectively with agglomerates of up to seven particles.

The works of Kim et al. [24] and Kalilainen et al. [22] suggested that adhesion effects under similar conditions as those used by Thatcher et al. [27] is plausible, although, no reported analysis on agglomerates was reported. In addition, particle seeding method used by Kim et al. [24] and Kalilainen et al. [22] who used the same DHC experimental setup differs from Thatcher et al. [27].

5. Conclusion

Using a one-way coupling between the carrier and the disperse phase, turbulent convective flow in a cubical cavity with two pairs of opposed thermally active walls at $Ra = 3.6 \times 10^9$ and suspended particle transport and deposition have been numerically investigated using DNS.

Temporal averages of the hydrodynamic field allowed to expand the correlations between the Rayleigh number and the wall-averaged Nusselt number derived by Fabregat and Pallares [18] up to 3.6×10^9 and to compare the present results with those available in the literature for a relatively wide range of Rayleigh numbers. Particle deposition rate on each cavity wall are reported and compared to the BL model and experimental results. The use of a disperse phase transport model accounting for hydrodynamic drag, buoyancy, lift, thermophoresis and Brownian effects is shown to accurately predict the wall deposition velocity for a relatively wide range of particle sizes ranging between thermophoresis and buoyancy dominated regimes at a relatively high Rayleigh number.

Results show that BL model is able to accurately predict deposition velocity of supermicron particles at $Ra = 3.6 \times 10^9$. For submicron particles there are differences compared with the DNS. This could be explained by the assumptions made in the derivation of the BL solutions. As a result, when the magnitude of the thermophoresis effect is similar to or larger than gravitational force, these models tend to over-predict the deposition on horizontal walls. DNS predictions of deposition velocity for supermicron particles are in excellent agreement with the experiment and BL model. Discrepancy appears when particles are less than one micron and thermophoresis is the dominating force. As suggested in the literature, this non-negligible difference with experiments for submicron particles could be explained considering the phenomenon of particle agglomeration (see Section 4).

Considering everything, our results suggest that the deposition of submicron particles is heavily influenced by thermophoretic forces. On the other hand, thermophoresis has negligible influence on deposition

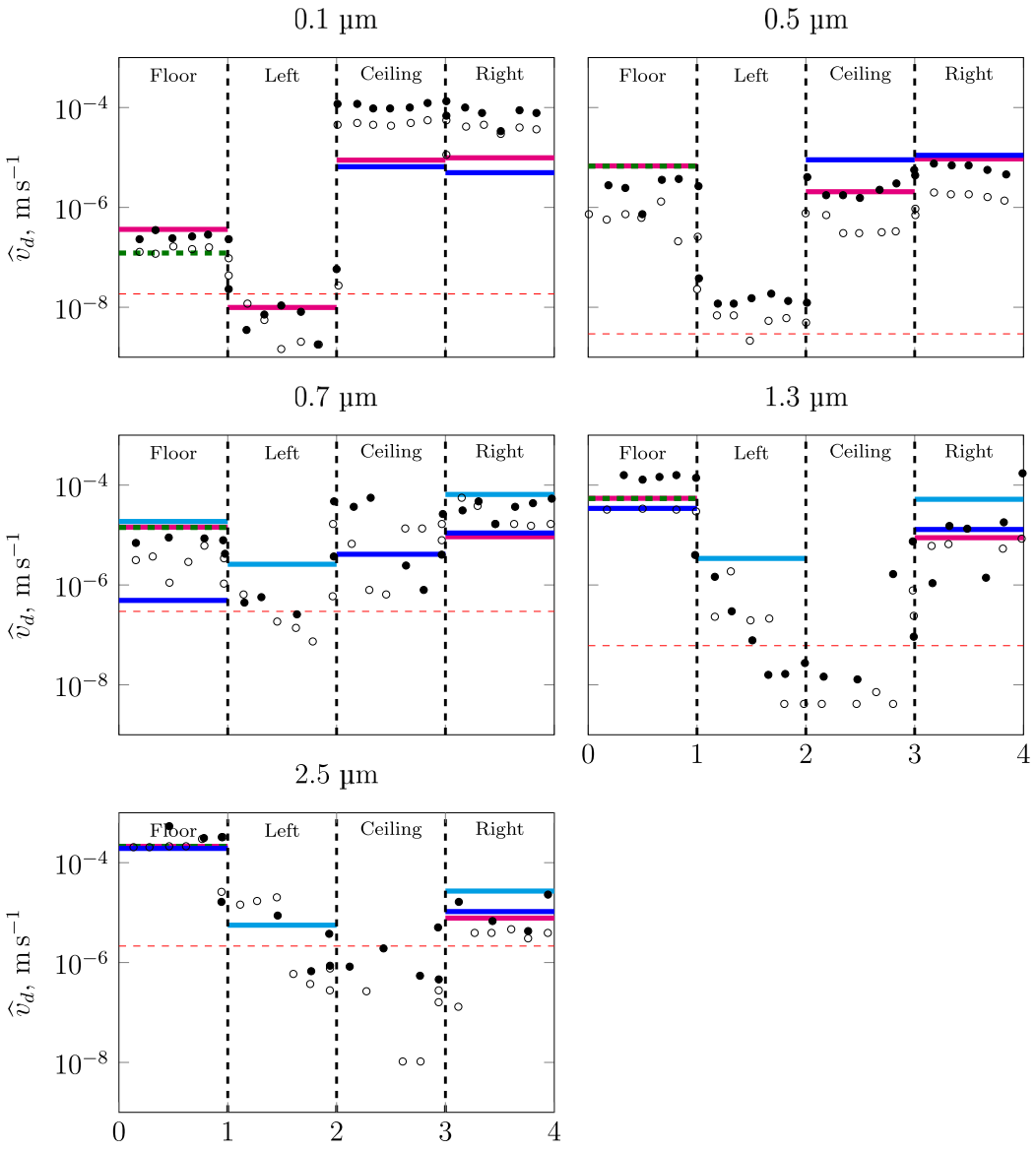

Fig. 13. Particle wall-average deposition velocity for all five diameters and four thermally active walls. Magenta and blue color represent BL model and DNS results, respectively. Dashed green line is the settling velocity. Red dashed line indicates the experimental detection level. Empty and filled round markers represent two different realisations of the experiment reported by Thatcher et al. [27]. Kim et al. [24] LES results are shown with teal lines.

Table 1

Buoyancy (n_g), horizontal ($n_{th}\frac{dT}{dx}$) and vertical ($n_{th}\frac{dT}{dy}$) thermophoresis terms for considered particle sizes.

$\widetilde{d}_p$, µm	n_g	$n_{th}\frac{dT}{dy}$	$n_{th}\frac{dT}{dx}$
0.1	−65.64	2165.03	1507.79
0.5	−65.64	84.41	58.79
0.7	−65.64	42.74	29.76
1.3	−65.64	11.97	8.34
2.5	−65.64	2.97	2.07

Table 2

Prescribed sizes vs. averaged particle fractions.

$\widetilde{d}_p$, µm	single fraction (%)	double fraction (%)	triple fraction (%)
0.5	72 ± 3	20 ± 2	8 ± 3
1.0	85 ± 3	13 ± 2	2 ± 1
2.5	90 ± 2	9 ± 3	1 ± 1

rate of particles larger than one micrometer for which buoyancy forces dominate the transport (see Table 2). A similar conclusion can be found in Dehbi et al. [23], Kim et al. [24] and Thatcher et al. [27].

Future efforts would be directed to use the present results to investigate the relative dispersion of particle pairs initialized within spheres approximately representing the aerosol cloud generated by a human exhalation. The goal is to obtain accurate estimates of the time required by such cloud to homogeneously disperse in a human-scale room. These results would be of help to characterize the infection risk from airborne contagious diseases including COVID-19 in closed room taking into account natural convection.

CRediT authorship contribution statement

Akim Lavrinenko: Conceptualization, Software, Validation, Investigation, Data-curation, Writing-original-draft, Writing-review-editing, Visualization. **Ferran Gisbert:** Software, Data-curation. **Jordi Pallares:** Conceptualization, Methodology, Software, Validation, Investigation, Resources, Writing-review-editing, Supervision, Project-

administration, Funding-acquisition. **Alexandre Fabregat:** Conceptualization, Methodology, Software, Investigation, Validation, Resources, Writing-review-editing, Supervision, Project-administration, Funding-acquisition.

Declaration of Competing Interest

The authors declare the following financial interests/personal relationships which may be considered as potential competing interests: Akim Lavrinenko reports financial support was provided by Spanish Ministerio de Ciencia.

Data availability

Data will be made available on request.

Acknowledgements

This work has been funded by Spanish Ministerio de Ciencia, Innovación y Universidades through the grants RTI2018-100907-A-I00 and PID2020-113303 GB-C21 and by the Generalitat de Catalunya through the grant 2017-SGR-1234.

References

[1] Cdc public health science agenda for covid-19. URL:https://www.cdc.gov/coronavirus/2019-ncov/science/science-agenda-covid19.html.
[2] Global research on coronavirus disease (covid-19). URL:https://www.who.int/emergencies/diseases/novel-coronavirus-2019/global-research-on-novel-coronavirus-2019-ncov.
[3] D.L. Liu, Particle deposition onto enclosure surfaces, Aerospace Report No TR-2009 (8550-2) (2009). URL:https://apps.dtic.mil/sti/pdfs/ADA505166.pdf.
[4] S. Muraoka, R. Takagi, Y. Araki, K. Uda, M. Sumitomo, S. Okamoto, M. Nishihori, T. Izumi, M. Nakamura, R. Saito, Blood flow stagnation after treatment of a giant internal carotid artery aneurysm: a computed fluid dynamics analysis, Sci. Rep. 12 (2022).
[5] J. Meyerjürgens, M. Ricker, V. Schakau, T.H. Badewien, E.V. Stanev, Relative dispersion of surface drifters in the north sea: the effect of tides on mesoscale diffusivity, J. Geophys. Res.: Oceans 125 (2020), https://doi.org/10.1029/2019JC015925.
[6] R. Puragliesi, A. Dehbi, E. Leriche, A. Soldati, M. Deville, DNS of buoyancy-driven flows and Lagrangian particle tracking in a square cavity at high Rayleigh numbers, Int. J. Heat Fluid Flow 32 (5) (2011) 915–931, https://doi.org/10.1016/j.ijheatfluidflow.2011.06.007. URL:https://www.sciencedirect.com/science/article/pii/S0142727X11000956.
[7] P.M. Doran, Chapter 9 - Heat Transfer, in: P.M. Doran (Ed.), Bioprocess Engineering Principles, (Second Edition), second edition Edition,, Academic Press, London, 2013, pp. 333–377, https://doi.org/10.1016/B978-0-12-220851-5.00009-5.
[8] A. Vasiliev, A. Sukhanovsky, P. Frick, A. Budnikov, V. Fomichev, M. Bolshukhin, R. Romanov, High rayleigh number convection in a cubic cell with adiabatic sidewalls, Int. J. Heat Mass Transf. 102 (2016) 201–212, https://doi.org/10.1016/j.ijheatmasstransfer.2016.06.015.
[9] I. Miroshnichenko, M. Sheremet, Turbulent natural convection heat transfer in rectangular enclosures using experimental and numerical approaches: A review, Renew. Sustain. Energy Rev. 82 (2018) 40–59, https://doi.org/10.1016/j.rser.2017.09.005. URL:https://www.sciencedirect.com/science/article/pii/S1364032117312595.
[10] S. Pandey, Y. Park, M. Ha, An exhaustive review of studies on natural convection in enclosures with and without internal bodies of various shapes, Int. J. Heat Mass Transf. 138 (2019) 762–795, https://doi.org/10.1016/j.ijheatmasstransfer.2019.04.097.
[11] A. Ammar, m.A. Isam, m.S. Nejla, An exhaustive review on natural convection within complex enclosures: Influence of various parameters, Chin. J. Phys. 74 (2021) 365–388, https://doi.org/10.1016/j.cjph.2021.10.012. URL:https://www.sciencedirect.com/science/article/pii/S0577907321002574.
[12] G.S. Shiralkar, C.L. Tien, A numerical study of the effect of a vertical temperature difference imposed on a horizontal enclosure, Numer. Heat Transf. 5 (2) (1982) 185–197, https://doi.org/10.1080/10407788208913442, arXiv.
[13] S. Ostrach, C. Raghavan, Effect of stabilizing thermal gradients on natural convection in rectangular enclosures, J. Heat Transfer 101 (2) (1979) 238–243, https://doi.org/10.1115/1.3450953, arXiv:https://asmedigitalcollection.asme.org/heattransfer/article-pdf/101/2/238/5744423/238_1.pdf.
[14] M. Corcione, Effects of the thermal boundary conditions at the sidewalls upon natural convection in rectangular enclosures heated from below and cooled from above, Int. J. Therm. Sci. 42 (2) (2003) 199–208, https://doi.org/10.1016/S1290-0729(02)00019-4. URL:https://www.sciencedirect.com/science/article/pii/S1290072902000194.
[15] M.E. Danis, M. Orhan, A. Ecder, Isph modelling of transient natural convection, Int. J. Comput. Fluid Dyn. 27 (1) (2013) 15–31, https://doi.org/10.1080/10618562.2012.753146, arXiv.
[16] K. Hanjalic, S. Vasić, Computation of turbulent natural convection in rectangular enclosures with an algebraic flux model, Int. J. Heat Mass Transf. 36 (1993) 3603–3624.
[17] A. Kirkpatrick, M. Bohn, An experimental investigation of mixed cavity natural convection in the high Rayleigh number regime, Int. J. Heat Mass Transf. 29 (1986) 369–382.
[18] A. Fabregat, J. Pallarès, Heat transfer and boundary layer analyses of laminar and turbulent natural convection in a cubical cavity with differently heated opposed walls, Int. J. Heat Mass Transf. 151 (2020), 119409, https://doi.org/10.1016/j.ijheatmasstransfer.2020.119409. URL:https://www.sciencedirect.com/science/article/pii/S001793101935731X.
[19] European Enviroment Agency, 3.3 dispersion of hazardous substances. URL: https://www.eea.europa.eu/publications/92-9157-202-0/page303.html.
[20] S. Ogbonnaya, O. Ajayi, Fouling phenomenon and its effect on heat exchanger: a review, Front. Heat Mass Transf. 9 (2017), https://doi.org/10.5098/hmt.9.31.
[21] Coronavirus disease (covid-19): How is it transmitted? URL:https://www.who.int/news-room/questions-and-answers/item/coronavirus-disease-covid-19-how-is-it-transmitted.
[22] J. Kalilainen, P. Rantanen, T. Lind, A. Auvinen, A. Dehbi, Experimental investigation of a turbulent particle-laden flow inside a cubical differentially heated cavity, J. Aerosol Sci. 100 (C) (2016) 73–87, https://doi.org/10.1016/j.jaerosci.2016.06.001.
[23] A. Dehbi, J. Kalilainen, T. Lind, A. Auvinen, A large eddy simulation of turbulent particle-laden flow inside a cubical differentially heated cavity, J. Aerosol Sci. 103 (2016), https://doi.org/10.1016/j.jaerosci.2016.10.003.
[24] H. Kim, A. Dehbi, J. Kalilainen, Measurements and LES computations of a turbulent particle-laden flow inside a cubical differentially heated cavity, Atmos. Environ. 186 (2018) 216–228, https://doi.org/10.1016/j.atmosenv.2018.05.037. URL: https://www.sciencedirect.com/science/article/pii/S1352231018303418.
[25] Alvin C.K. Lai, Miriam A. Byrne, Antony J.H. Goddard, Experimental studies of the effect of rough surfaces and air speed on aerosol deposition in a test chamber, Aerosol Sci. Technol. 36 (10) (2002) 973–982, https://doi.org/10.1080/02786820290092249, arXiv.
[26] X. Zhong, S.C. Fu, K.C. Chan, C.Y. Chao, Experimental study of particle deposition on patterned microstructured surfaces in a chamber environment, J. Aerosol Sci. 157 (2021), 105802, https://doi.org/10.1016/j.jaerosci.2021.105802. URL: https://www.sciencedirect.com/science/article/pii/S0021850221005346.
[27] T.L. Thatcher, W.A. Fairchild, W.W. Nazaroff, Particle deposition from natural convection enclosure flow onto smooth surfaces, Aerosol Sci. Technol. 25 (4) (1996) 359–374, https://doi.org/10.1080/02786829608965402.
[28] J. Pallares, A. Fabregat, Prediction of particle deposition on the walls of a cubical cavity with differentially heated opposed walls using heat and mass transfer laminar mixed convection boundary layer models, Int. J. Heat Mass Transf. 165 (2021), 120691, https://doi.org/10.1016/j.ijheatmasstransfer.2020.120691. URL: https://www.sciencedirect.com/science/article/pii/S0017931020336279.
[29] A. Fabregat, J. Pallarès, Transport and wall surface deposition of airborne particles in enclosed, buoyancy-driven turbulent flows using fully-resolved numerical simulations, Int. Commun. Heat Mass Transfer 134 (2022), 106048, https://doi.org/10.1016/j.icheatmasstransfer.2022.106048. URL:https://www.sciencedirect.com/science/article/pii/S0735193322001701.
[30] P.F. Fischer, J.W. Lottes, S.G. Kerkemeier, Nek5000. URL:http://nek5000.mcs.anl.gov.
[31] M.O. Deville, P.F. Fischer, E.H. Mund, D.K. Gartling, High-Order Methods for Incompressible Fluid Flow, Appl. Mech. Rev. 56 (3) (2003), https://doi.org/10.1115/1.1566402. B43–B43. arXiv:https://asmedigitalcollection.asme.org/appliedmechanicsreviews/article-pdf/56/3/B43/5439822/b34_1.pdf.
[32] K. Mittal, S. Dutta, P. Fischer, Multirate timestepping for the incompressible navier-stokes equations in overlapping grids, J. Comput. Phys. 437 (2021), 110335, https://doi.org/10.1016/j.jcp.2021.110335. URL:https://www.sciencedirect.com/science/article/pii/S0021999121002308.
[33] A. Fabregat Tomàs, A.C. Poje, T.M. Özgökmen, W.K. Dewar, Dynamics of multiphase turbulent plumes with hybrid buoyancy sources in stratified environments, Phys. Fluids 28 (9) (2016), 095109, https://doi.org/10.1063/1.4963313 arXiv.
[34] E. Merzari, A. Obabko, P. Fischer, Spectral element methods for liquid metal reactors applications (2017). doi:10.48550/ARXIV.1711.09307. URL:https://arxiv.org/abs/1711.09307.
[35] R. Vinuesa, P. Negi, M. Atzori, A. Hanifi, D. Henningson, P. Schlatter, Turbulent boundary layers around wing sections up to rec=1,000,000, Int. J. Heat Fluid Flow 72 (2018) 86–99, https://doi.org/10.1016/j.ijheatfluidflow.2018.04.017. URL: https://www.sciencedirect.com/science/article/pii/S0142727X17311426.
[36] J. Scheel, S. Emran, J. Schumacher, Resolving the fine-scale structure in turbulent Rayleigh-Benard convection, New J. Phys. 15 (2013), https://doi.org/10.1088/1367-2630/15/11/113063.
[37] M.D. Allen, O.G. Raabe, Slip correction measurements of spherical solid aerosol particles in an improved millikan apparatus, Aerosol Sci. Technol. 4 (3) (1985) 269–286, https://doi.org/10.1080/02786828508959055, arXiv.
[38] L. Talbot, R.K. Cheng, R.W. Schefer, D.R. Willis, Thermophoresis of particles in a heated boundary layer, J. Fluid Mech. 101 (4) (1980) 737–758, https://doi.org/10.1017/S0022112080001905.
[39] J.B. McLaughlin, Inertial migration of a small sphere in linear shear flows, J. Fluid Mech. 224 (1991) 261–274, https://doi.org/10.1017/S0022112091001751.

[40] H. Ounis, G. Ahmadi, J.B. McLaughlin, Brownian particle deposition in a directly simulated turbulent channel flow, Physics of Fluids A, Fluid Dyn. 5 (6) (1993) 1427–1432, https://doi.org/10.1063/1.858578, arXiv.
[41] I.E. Barton, Exponential-lagrangian tracking schemes applied to stokes law, J. Fluids Eng. 118 (1996) 85–89.
[42] W.W. Nazaroff, G.R. Cass, Environ. Int. 15 (1989) 567–584.